



HAL
open science

Highly heterogeneous mantle caused by recycling of oceanic lithosphere from the mantle transition zone

Shengping Qian, Vincent Salters, Alex J. Mccoy-West, Jonny Wu, Estelle F. Rose-Koga, Alexander R. L. Nichols, Le Zhang, Huaiyang Zhou, Kaj Hoernle

► **To cite this version:**

Shengping Qian, Vincent Salters, Alex J. Mccoy-West, Jonny Wu, Estelle F. Rose-Koga, et al.. Highly heterogeneous mantle caused by recycling of oceanic lithosphere from the mantle transition zone. *Earth and Planetary Science Letters*, 2022, 593, 10.1016/j.epsl.2022.117679 . insu-03777180

HAL Id: insu-03777180

<https://insu.hal.science/insu-03777180>

Submitted on 6 Oct 2023

HAL is a multi-disciplinary open access archive for the deposit and dissemination of scientific research documents, whether they are published or not. The documents may come from teaching and research institutions in France or abroad, or from public or private research centers.

L'archive ouverte pluridisciplinaire **HAL**, est destinée au dépôt et à la diffusion de documents scientifiques de niveau recherche, publiés ou non, émanant des établissements d'enseignement et de recherche français ou étrangers, des laboratoires publics ou privés.

1 **Highly heterogeneous mantle caused by recycling of oceanic**
2 **lithosphere from the mantle transition zone**

3
4 Shengping Qian^{1*}, Vincent Salters², Alex J. McCoy-West³, Jonny Wu⁴, Estelle F.
5 Rose-Koga⁵, Alexander R. L. Nichols⁶, Le Zhang⁷, Huaiyang Zhou^{1*}

6 ¹State Key Laboratory of Marine Geology, Tongji University, Shanghai, China

7 ²Dept. of Earth Ocean and Atmospheric Science and NHMFL, Florida State
8 University, Tallahassee, USA

9 ³Isotopics Geochemistry Laboratory, School of Earth and Environmental Science,
10 James Cook University, Townsville, Australia

11 ⁴Dept. of Earth & Atmospheric Sciences, University of Houston, Houston, USA

12 ⁵Université Clermont Auvergne, CNRS, IRD, OPGC, Laboratoire Magmas et Volcans,
13 F-63000 Clermont-Ferrand, France

14 ⁶School of Earth and Environment, University of Canterbury, Private Bag 4800,
15 Christchurch 8140, New Zealand

16 ⁷State Key Laboratory of Isotope Geochemistry, Guangzhou Institute of
17 Geochemistry, Chinese Academy of Sciences, Guangzhou, China

18

19 * Corresponding author: shengpingqian@tongji.edu.cn and zhouhy@tongji.edu.cn

20 **Abstract**

21 Geochemical heterogeneities observed in the mantle are usually attributed to
22 recycling of oceanic lithosphere through subduction. However, it remains hotly
23 debated where recycled material stagnates, and how quickly it can be liberated back to
24 surface. This knowledge gap hinders our understanding of mantle circulation and the
25 chemical evolution of the Earth. Here we address these questions using a combination
26 of geochronology and geochemistry from South China Sea (SCS) seamounts. The
27 Shixingbei seamount lavas formed during active seafloor spreading at c. 19.1 Ma
28 show limited geochemical variability, whereas the Zhenbei-Huangyan seamount chain
29 formed during the post-spreading stage at c. 7.8 Ma and displays a wide range of
30 compositions. However, melt inclusions in olivine and plagioclase from the
31 Zhenbei-Huangyan basalts show considerably greater isotopic variability than seen in
32 the whole rock compositions of both the SCS syn- and post-spreading lavas. A
33 previously unidentified third mantle source component (FOZO) revealed by
34 olivine-hosted melt inclusions along with both depleted (DMM) and enriched (EMII)
35 mantle components is required in the source region to explain the observed isotopic
36 and chemical variability. On the basis of our results, the age of the recycled ocean
37 crust and sediments in this region are estimated to be c. 120 – 350 Ma. We infer that
38 these enriched components in the SCS lavas come from the mantle transition zone.
39 Variations in mantle source heterogeneity coupled with melting process control
40 spatial–temporal (spreading vs. post-spreading stage) geochemical variations of lavas

41 from the SCS and surrounding areas. Together with the results from published studies,
42 we propose that marginal basins are one of the major locations on Earth where
43 oceanic and/or continental lithosphere are transferred into the upper mantle and
44 transition zone, representing an important source of upper mantle heterogeneity. We
45 provide a simple conceptual model linking plate subduction and upper mantle
46 heterogeneity and the volcanism in the SCS and surrounding areas.

47

48 **Keywords**

49 South China Sea; mantle transition zone; recycled oceanic crust; EMII and FOZO;
50 mantle heterogeneity

51

52 **1. Introduction**

53 In general, mid-ocean ridge basalts (MORBs) have relatively uniform and
54 overall depleted compositions, while oceanic island basalts (OIBs) display
55 considerable chemical heterogeneity (e.g., Gale et al., 2013; Hoernle et al., 2011;
56 Hofmann, 1997; Jackson and Hart, 2006; Salters and Stracke, 2004; Stracke et al.,
57 2005). Five endmembers are commonly proposed to explain the isotopic
58 heterogeneity observed in oceanic rocks: depleted MORB-source mantle (DMM),
59 enriched mantle one (EMI) and two (EMII), high time-integrated μ ($^{238}\text{U}/^{204}\text{Pb}$)
60 mantle (HIMU), and a focal zone (FOZO) component (e.g., Hanan and Graham,
61 1996; Hickey-Vargas, 1992; Stracke et al., 2005; Workman and Hart, 2005; Zindler

62 and Hart, 1986). The cause of the geochemical differences between MORBs and OIBs
63 and the chemical heterogeneity of Earth's mantle is mainly attributed to mantle
64 convection, but the understanding of where recycled material stagnates and how it is
65 mingled and arrives back at the surface, is still debated.

66 MORBs originate from a large-scale homogeneous, incompatible element-poor
67 shallow and degassed mantle, whereas OIBs are related to mantle plumes sampling
68 both ancient undegassed domains and recycled crustal reservoirs (e.g., Castillo et al.,
69 2010; Hofmann, 1997; Jackson and Hart, 2006; McCoy-West et al., 2016; Salters and
70 Stracke, 2004; Stracke et al., 2005; Workman and Hart, 2005; Zindler and Hart,
71 1986). Nevertheless, the two-layer mantle convection regime proposed based on
72 geochemical data (e.g., Hofmann, 1997) is hard to reconcile with geophysical
73 observations for whole-mantle convection (van der Hilst et al., 1997). Alternatively, a
74 ubiquitous distribution of small- to moderate-scale heterogeneity in the upper mantle
75 is considered to be responsible for geochemical variability of MORBs and OIBs
76 (Castillo et al., 2010; Meibom and Anderson, 2004).

77 The South China Sea (SCS), one of the marginal basins in the western Pacific,
78 formed by seafloor spreading between 33 – 15 Ma (Li et al., 2014). During the period
79 of SCS seafloor spreading, magmatic activities primarily occurred in the SCS basin
80 and southeast China, then, after cessation of SCS seafloor spreading, intraplate
81 volcanism was widely distributed in the SCS basin and adjacent areas (such as
82 southeast (SE) China, the Pearl River basin, and Indochina; **Fig. 1**) (Wang et al.,

83 2013; Zou and Fan, 2010). Previous studies show remarkable differences between the
84 geochemical compositions of the spreading stage MORBs and post-spreading
85 seamount lavas (Qian et al., 2021). However, the causes of these remain unclear. In
86 addition, it remains unclear why volcanism after cessation of spreading is widespread
87 in the SCS and surrounding areas.

88 Although bulk-rock geochemistry of mafic volcanic rocks is commonly used to
89 evaluate the geochemical heterogeneity of the mantle, most magmas that reach the
90 surface represent complex mixtures of melts, which through their homogenization and
91 re-equilibration with the surrounding mantle at shallower depths effectively erase
92 much of their original source heterogeneity (Kamenetsky et al., 1997; Kent, 2008;
93 Peate et al., 2012). Detailed studies of individual rock samples, especially of the
94 isotopic composition of their various constituents, including crystal cargo and melt
95 inclusions trapped in the crystals, can be used to assess the heterogeneity of the
96 underlying mantle source (e.g., Hanyu et al., 2019; Jackson and Hart, 2006;
97 Kamenetsky et al., 1997; Kent, 2008; Qian et al., 2017; Ramos and Tepley III, 2008;
98 Rose-Koga et al., 2017; Sobolev et al., 2011). In this study we examine the age and
99 geochemistry (whole rock; matrix glass; olivine (ol), clinopyroxene (cpx) and
100 plagioclase (plag) crystal; and ol and plag-hosted melt inclusion compositions) of the
101 lavas from the syn-spreading Shixingbei seamount, and post-spreading
102 Zhenbei-Huangyan seamount chain in the SCS (**Fig. 1**). Our results display
103 considerably larger isotopic variability than observed previously from whole rocks

104 analyses, pointing to mantle source heterogeneity beneath the SCS resulting from
105 recycling of oceanic crust and sediments. The enriched mantle reservoirs are most
106 likely introduced from the mantle transition zone (MTZ) into the upper mantle. Based
107 on the temporal-spatial evolution of volcanism and our new geochemical and
108 geophysical evidence, we propose that the Cenozoic magmatism in SE Asia is
109 generated by active upwelling of mantle material linked to curved subduction
110 systems.

111

112 **2. Geological setting and samples**

113 The SCS is one of the largest marginal seas in the western Pacific (~3,500,000
114 km²), with the Eurasian plate to the north, the Philippine Sea plate to the east, the
115 Australian plate to the south, and the Indian plate (or Indochina block) to the west
116 (**Fig. 1**). The SCS developed as a result of multiple episodes of continental rifting and
117 seafloor spreading during the Cenozoic (Briaies et al., 1993; Li et al., 2014; Sibuet et
118 al., 2016). The deep-water basin of the SCS comprises three parts, the East Sub-basin
119 (ESB), Southwest Sub-basin (SWSB) and Northwest Sub-basin (NWSB) (**Fig. 1**).
120 Constrained by mapping magnetic anomalies and cores recovered from the
121 International Ocean Discovery Program (IODP) Expedition 349 (microfossil age
122 constraints), seafloor spreading started 33 Ma near the northern continental margin of
123 the SCS (corresponding to the oldest seafloor spreading magnetic anomaly C12), and
124 ceased at c. 15 Ma in the ESB and c.16 Ma in the SWSB (Li et al., 2014). Late

125 Cenozoic volcanism is widespread and a prominent feature in SE Asia (including
126 SCS, SE China, and Indochina Peninsula), with the majority of magmatism younger
127 than sea-floor spreading in the SCS (between c. 33 and 16 Ma) (e.g., Hoang &
128 Flower, 1998; Wang et al., 2013; Yan et al., 2018; Zou and Fan, 2010). The SCS and
129 nearby areas are surrounded by several subduction zones (**Fig. 1**), indicating that the
130 volcanism in SE Asia took place in the same tectonic setting. In addition, the SCS
131 post-spreading seamount lavas and synchronous intraplate lavas in SE China and
132 Indochina Peninsula share similar chemical and isotopic characteristics with typical
133 E-MORB to OIB-type incompatible element distributions, and distinctive Pb isotope
134 compositions similar to EMII-type OIB (e.g., Hoang & Flower, 1998; Qian et al.,
135 2021; Wang et al., 2013; Yan et al., 2018; Zou and Fan, 2010), suggesting a common
136 mantle source.

137 The SCS preserves both seafloor spreading and post-spreading volcanic features.
138 Seafloor spreading stage seamounts are mostly distributed in the northern SCS;
139 post-spreading stage volcanism is more extensive in the SCS basin and predominantly
140 occurs in ESB and SW SCS basin, such as two north-south trending seamount chains
141 (Longbei and Longnan seamounts; Nanyue and Beiyue seamounts) in the SWSB, and
142 an east-west trending Zhenbei-Huangyan seamount chain in ESB. The samples for
143 this study were collected from Shixingbei seamount, which is not in a chain, and the
144 Zhenbei-Huangyan seamount chain in the SCS (**Fig. 1**) with the ROPOS remotely
145 operated subsea vehicle operated by the Canadian Scientific Submersible Facility

146 (Fig. S1). Shixingbei seamount lies in the middle of the SCS Basin (Fig. 1). The
147 Zhenbei and Huangyan seamounts formed after seafloor spreading ceased in the ESB
148 and are aligned northeastwards from the fossil spreading ridge (Li et al., 2014) (Fig.
149 1). Most lavas from these seamounts display pillow structures with columnar jointing
150 (Fig. S1c and d). The basalts from the SCS seamounts are typically variably vesicular
151 and porphyritic (3-20 %) with phenocrysts dominated by olivine (ol), clinopyroxene
152 (cpx) and plagioclase (plag) (Fig. S2a, b, c, d, e). In some samples, ol crystals contain
153 spinels (Fig. S2a, b), and ol and plag crystals also contain melt inclusions up to 140
154 μm in size (Fig. S2c, e). Biotite is found in rare evolved samples (such as trachytes),
155 in which alkali-feldspar and cpx dominate the phenocryst assemblage (Fig. S2f).

156

157 3. Analytical methods

158 Complete description of the analytical techniques can be found in the
159 supplementary material and are briefly discussed here. Plag separates from two
160 samples (2061-R7 from Shixingbei seamount and 2055-R12 from Huangyan
161 seamount) were selected for Ar-Ar age determinations by an ARGUS-VI
162 multi-collector instrument at the Argon geochronology laboratory of the Oregon State
163 University.

164 A U-Pb age on zircon from trachyte 2059-R16 from Zhenbei seamount was
165 dated using a Thermo Element XR instrument connected to a RESOLUTION M-50 laser
166 at Guangzhou Institute of Geochemistry, Chinese Academy of Science (GIG-CAS).

167 Major and trace elements of the SCS seamount whole-rock samples were analyzed
168 using a PANalytical AXIOS-Advanced X-ray fluorescence spectrometer at the State
169 Key Laboratory of Marine Geology (SKLMG) in Tongji University, and an Agilent
170 7900 inductively coupled plasma-mass spectrometer (ICP-MS) at GIG-CAS,
171 respectively. The whole-rock Sr–Nd–Pb isotopes of volcanic samples were analyzed
172 using a Neptune Plus multi-collector (MC-)ICP-MS at GIG-CAS. Major and trace
173 elements of minerals and glasses (matrix glass and melt inclusion) were analyzed
174 using a JEOL JXA-8230 electron probe micro-analyzer at SKLMG in Tongji
175 University and an excimer 193 nm laser ablation system (RESOLUTION M-50) coupled
176 to a Thermo Element ICP-MS instrument at GIG-CAS, respectively. In situ Sr–Pb
177 isotopes of feldspar, matrix glass and melt inclusion were analyzed using a Neptune
178 Plus MC-ICP-MS with a RESOLUTION M-50 laser at GIG-CAS.

179

180 **4. Results**

181 *4.1 Geochronology*

182 Some samples described here were collected from Shixingbei seamount (**Fig. 1**),
183 and the age of volcanism at these sites was unknown prior to this study. Plag in
184 volcanic rock sample 2061-R7 from the Shixingbei seamount yield a $^{40}\text{Ar}/^{39}\text{Ar}$
185 plateau age of 19.10 ± 0.78 Ma (**Fig. 2A**), indicating the off-axis Shixingbei seamount
186 formed during the syn-spreading stage (33 – 16 Ma) of the SCS. The two lavas from
187 the Huangyan and Zhenbei seamounts in the SCS ESB yielded significantly younger

188 ages. Sample 2055-R12 from the Huangyan seamount gave a $^{40}\text{Ar}/^{39}\text{Ar}$ plateau age of
189 7.78 ± 0.21 Ma (**Fig. 2B**), which affirms a previously published K-Ar age data ($7.77 \pm$
190 0.49 Ma) for samples from the same seamount (Wang et al., 2009). U–Pb dating of
191 zircon grains from the Zhenbei seamount trachyte 2059-R16 yields a weighted mean
192 $^{206}\text{Pb}/^{238}\text{U}$ age of 7.76 ± 0.13 Ma ($n = 31$; **Fig. 2C**). The Zhenbei-Huangyan seamount
193 chain samples are nearly age-synchronous and do not show clear age progression.
194 Thus, the available data indicate that the Shixingbei seamount formed while seafloor
195 spreading was still active in the SCS, whereas the Zhenbei-Huangyan seamount lavas
196 formed after spreading ceased.

197

198 *4.2 Geochemistry*

199 The studied Shixingbei seamount and Zhenbei-Huangyan seamount chain lavas
200 show temporal variations in geochemical compositions. The Shixingbei seamount
201 lavas formed during the SCS spreading stage are tholeiitic basalts (alkalis ($\text{Na}_2\text{O} +$
202 K_2O) = $3.03 - 3.59$; $\text{SiO}_2 = 49.59 - 51.32$; $\text{MgO} = 4.90 - 5.93$; all oxide contents in
203 weight % normalized to 100% on volatile-free basis), and possess similar major
204 element compositions to spreading stage MORBs sampled by IODP Expedition 349
205 within the SCS basin (**Fig. 3**).

206 The post-spreading Zhenbei-Huangyan seamount lavas range from alkali basalt
207 through trachyte ($\text{SiO}_2 = 45.2 - 62.7$; $\text{MgO} = 9.6 - 0.7$) to basanite ($\text{SiO}_2 = 43.4 -$
208 44.4 ; $\text{MgO} = 10.4 - 11.8$) (**Fig. 3**). MgO is highest in ol-hosted melt inclusions ($7.2 -$

209 11.9), intermediate in plag-hosted melt inclusions (4.5 – 6.3) and lowest in matrix
210 glass (2.2 – 4.6) (**Fig. 3B**). As MgO decreases in ol-hosted melt inclusions, whole
211 rocks and matrix glass with MgO > 4.5, both SiO₂, and Al₂O₃ increase and FeO^t (t =
212 total) decrease overall (**Fig. 3**), reflecting an assemblage dominated by ol, cpx and
213 Fe-oxide fractionation. Plag melt inclusions and matrix glass with MgO < 4.5 (**Fig. 3**),
214 however, are shifted to lower Al₂O₃ and Na₂O and higher FeO^t, consistent with plag
215 joining the fractionating phases. Ol have relatively high CaO (0.16 – 0.35 wt.%)
216 (**Table S5**), favoring crystallization from mafic melts rather than being xenocrysts
217 from mantle peridotite (Qian et al., 2021). Cpx have diopsidic to augitic compositions
218 (En₃₅₋₄₄Fs₁₁₋₂₀Wo₄₁₋₄₈) with relatively high Mg# ($100\text{Mg}/(\text{Mg}+\text{Fe}^{+2}) = 63 - 80$; **Table**
219 **S3**). Plag range from bytownite to andesine (An₅₇₋₇₅; **Table S4**).

220 The Zhenbei-Huangyan seamount whole rock lavas, matrix glass and plag-hosted
221 melt inclusions have incompatible element contents characteristic of intraplate
222 volcanic rocks, showing overall enrichment in highly to moderately incompatible
223 elements, slight relative Nb enrichment and relative K and Pb depletion (**Fig. 4A, B**).
224 Notably, the SCS Shixingbei seamount tholeiitic basalts have significantly lower
225 incompatible trace element concentrations than the Zhenbei-Huangyan seamount
226 lavas (**Fig. 4A**), but slightly higher incompatible trace element concentrations than
227 MORBs erupted during the SCS spreading stage (**Fig. 4A**). They also have lower
228 La/Sm, Sm/Yb, and Nb/Zr than the Zhenbei-Huangyan seamount lavas (**Fig. 4C, D**).

229 The Shixingbei tholeiitic basalts ($n = 4$) formed during the SCS spreading stage
230 have less radiogenic $^{87}\text{Sr}/^{86}\text{Sr}$ (0.7033 – 0.7034) and $^{206}\text{Pb}/^{204}\text{Pb}$ (18.537 – 18.571),
231 and more radiogenic ϵ_{Nd} (5.2 – 5.4) than the Zhenbei-Huangyan lavas ($^{87}\text{Sr}/^{86}\text{Sr} =$
232 0.7035 – 0.7043, $^{206}\text{Pb}/^{204}\text{Pb} = 18.591 – 18.809$, and $\epsilon_{\text{Nd}} = 3.2 – 4.8$) (**Fig. 5**). In
233 general, matrix glass ($^{87}\text{Sr}/^{86}\text{Sr} = 0.7036 – 0.7039$; $^{207}\text{Pb}/^{206}\text{Pb} = 0.832 – 0.838$;
234 $^{208}\text{Pb}/^{206}\text{Pb} = 2.092 – 2.098$) and plag ($^{87}\text{Sr}/^{86}\text{Sr} = 0.7035 – 0.7041$; $^{207}\text{Pb}/^{206}\text{Pb} =$
235 0.828 – 0.843; $^{208}\text{Pb}/^{206}\text{Pb} = 2.054 – 2.111$) within the Zhenbei-Huangyan seamounts
236 show a similar range of Sr-Pb isotope compositions as those exhibited by the whole
237 rocks ($^{87}\text{Sr}/^{86}\text{Sr} = 0.7035 – 0.7043$; $^{207}\text{Pb}/^{206}\text{Pb} = 0.831 – 0.838$; $^{208}\text{Pb}/^{206}\text{Pb} = 2.079 –$
238 2.090) (**Fig. 6; Table S1, S2 and S4**). Plag-hosted melt inclusions extend to much
239 more radiogenic Sr ($^{87}\text{Sr}/^{86}\text{Sr} = 0.7037 – 0.7067$) (**Fig. 6; Table S2**). Ol-hosted melt
240 inclusions extend to considerably more radiogenic Sr ($^{87}\text{Sr}/^{86}\text{Sr} = 0.7028 – 0.7062$)
241 and Pb ($^{207}\text{Pb}/^{206}\text{Pb} = 0.778 – 0.856$; $^{208}\text{Pb}/^{206}\text{Pb} = 1.959 – 2.099$) isotopes (**Fig. 6;**
242 **Table S2**). The melt inclusions in the most forsteritic ol (Fo_{88-89}) have more
243 radiogenic Pb isotope ratios ($^{207}\text{Pb}/^{206}\text{Pb} = 0.778 – 0.807$; $^{208}\text{Pb}/^{206}\text{Pb} = 1.958 – 2.035$)
244 than melt inclusions in Fo_{82-87} ol ($^{207}\text{Pb}/^{206}\text{Pb} = 0.816 – 0.856$; $^{208}\text{Pb}/^{206}\text{Pb} = 2.050 –$
245 2.099) (**Table S2**). Two melt inclusions in the same ol crystal have different $^{87}\text{Sr}/^{86}\text{Sr}$
246 (0.70581 for 2055-R7-28MI1, 0.70658 for 2055-R7-28MI2) (**Tables S2**).

247

248 5. Discussion

249 5.1 A three component mixing model for SCS seamount lava genesis

250 The SCS seamount lavas have a large range in Pb, Sr and Nd isotope
251 compositions (**Fig. 5**). It is critical to determine if this isotopic variability reflects a
252 heterogeneous source, or whether crustal contamination during magma ascent and
253 emplacement has modified the isotopic signal. Since $^{87}\text{Sr}/^{86}\text{Sr}$ ratios in 6 – 15 Ma
254 oceanic crust (e.g. IODP sites 504 and 1256) (Höfig et al., 2014) generally do not
255 exceed 0.7040 (only ~5%), assimilation of in-situ altered oceanic crust is unlikely to
256 generate the radiogenic $^{87}\text{Sr}/^{86}\text{Sr}$ (extending to 0.7067) observed for lavas from the
257 SCS and surrounding areas. Sediment assimilation is also unlikely due to the paucity
258 of sediment (< 10 m) on the seafloor at the time the seamounts formed (Li et al.,
259 2014). It is noteworthy that the isotope systematics of most of these lavas do not
260 appear to be significantly affected by crustal assimilation, as suggested by isotope
261 ratios being mostly independent of the degree of differentiation (e.g. MgO, Mg/Si,
262 Mg# and/or Fo content) (**Fig. S6**). In addition, the SCS seamount lava and most
263 intraplate lava samples with high- ϵ_{Nd} (> 2.7) from the SE Asia have a large variation
264 in Nb/U with no correlations with ϵ_{Nd} , indicating insignificant crustal contamination
265 (**Fig. S6**). By contrast, the low- ϵ_{Nd} (< 2.7) lavas (mainly from the Indochina
266 Peninsula; Wang et al., 2013) show strong covariation between Mg/Si, Nb/U, and ϵ_{Nd}
267 (**Fig. S6**), indicating that they are most likely affected by crustal contamination.

268 Lava whole rock compositions are commonly assumed to represent melt
269 compositions (possibly, except for melt volatile element compositions), implying that
270 minerals crystallized from that melt should inherit the whole rock composition. This

271 assumption, however, is not valid for the Zhenbei-Huangyan lavas. The most mafic
272 (MgO = 10.4 – 11.8) basanitic lavas represent complex mixtures of evolved basaltic
273 melt (matrix glass with Mg# ($100 \text{ Mg}/(\text{Mg} + \text{Fe}^{2+})$) = 32 – 44) and a complex crystal
274 cargo, primarily mafic ol (Fo_{82–89}) and cpx (Mg# = 63 – 80) but also Fe oxides and
275 plag. Plag have major element and Sr-Pb isotopic compositions compatible with being
276 phenocrysts because their isotopic compositions are similar to those of their host
277 whole rocks. The plag- and ol-hosted melt inclusions, on the other hand, show a large
278 variation in Sr isotopes and record interaction with an EMII-like component with
279 radiogenic $^{87}\text{Sr}/^{86}\text{Sr}$ (≥ 0.7067) (**Fig. 6**). In addition, the plag- and ol- melt inclusions
280 have higher MgO contents and show larger variations in isotopic compositions
281 compared to the matrix glasses (**Fig. 3, 6**). Ol, thus, must have crystallized from more
282 mafic melts than the matrix glasses (**Fig. 3, 6**).

283 Whole rock Sr-Nd-Pb isotope compositions of post-spreading lavas from the
284 SCS and nearby areas (SE China and Indochina) (**Fig. 5**) have previously been
285 explained by mixing of at least two major components: depleted upper mantle or the
286 SCS spreading lavas and an EMII-like component (Wang et al., 2013; Zou and Fan,
287 2010). However, this two-component mixing model does not adequately explain the
288 isotope compositions of ol and plag-hosted melt inclusions from Zhenbei-Huangyan
289 seamounts (**Fig. 6**). Instead, they require mixing of at least three distinct components
290 (**Fig. 6**):

291 **1) DMM:** Zhenbei ol-hosted (Fo₈₃₋₈₄) melt inclusions and IODP Site U1431
292 MORB lavas (Zhang et al., 2018) have non-radiogenic Sr ($^{87}\text{Sr}/^{86}\text{Sr} \leq 0.7029$) and
293 moderate radiogenic Pb ($^{207}\text{Pb}/^{206}\text{Pb} > 0.86$; $^{208}\text{Pb}/^{206}\text{Pb} \geq 2.10$) isotopes,
294 characteristic of a depleted upper mantle MORB type source;

295 **2) FOZO:** Huangyan melt inclusions hosted in magnesium-rich ol (Fo₈₈₋₈₉) in
296 equilibrium with mantle peridotite have non-radiogenic Sr ($^{87}\text{Sr}/^{86}\text{Sr} = 0.7036 -$
297 0.7037) and radiogenic Pb ($^{207}\text{Pb}/^{206}\text{Pb} = 0.78 - 0.81$; $^{208}\text{Pb}/^{206}\text{Pb} = 1.96 - 2.03$)
298 isotopes. They are similar to the FOZO component ubiquitous in mid-ocean-ridge and
299 intraplate basalts (Hanan and Graham, 1996; Stracke et al., 2005);

300 **3) EMII:** Huangyan melt inclusions hosted in plag and some ol (at least three ol
301 crystals) require a component with the most radiogenic Sr ($^{87}\text{Sr}/^{86}\text{Sr} \geq 0.7067$) and
302 moderately radiogenic Pb ($^{207}\text{Pb}/^{206}\text{Pb} = 0.826 - 0.845$; $^{208}\text{Pb}/^{206}\text{Pb} = 2.06 - 2.10$)
303 isotopes.

304 Clearly, plag and ol crystals crystallizing from the same magma batch should
305 possess identical isotopic compositions, therefore the large range of plag- and
306 ol-hosted melt inclusions compositions seen in the SCS seamount lavas (i.e. **Fig. 6**)
307 requires trapping melts of isotopically distinct parental magmas (Qian et al., 2017;
308 Ramos and Tepley Iii, 2008; Rose-Koga et al., 2017). The FOZO-like signature in
309 particular is only clearly identified in a few ol-hosted melt inclusions, implying that
310 the proportion of the FOZO component contributing to erupted lavas must be small,
311 and/or that the FOZO-like fragments in the mantle are so small that they are rarely

312 sampled in melt inclusions. They are probably present in the whole rock, but they are
313 so diluted that the FOZO “flavor” cannot be distinguished. It is apparent that
314 shallow-level storage and magma mixing resulted in dilution of the FOZO component
315 in the SCS seamount lavas, before eruption.

316

317 *5.2 Rapid recycling of slab-derived source components*

318 We now discuss the possible origin of the enriched components (EMII and
319 FOZO) necessary to explain the isotopic variations of the crystals and their MIs in the
320 SCS (**Fig. 6**). Some plag- and ol-hosted melt inclusions have more radiogenic
321 $^{87}\text{Sr}/^{86}\text{Sr}$ than matrix glasses and plag crystals, and form mixing arrays between
322 SCS-spreading or Pacific MORBs and EMII (**Fig. 6**). A potential source component
323 for EMII is delaminated lower crustal material, but the $\text{H}_2\text{O}/\text{Ce}$ ratios of the SCS
324 seamount lavas are much higher than those of lower continental crust (LCC) granulite
325 xenoliths from SE Asia (Qian et al., 2021). In addition, the LCC has higher $^{87}\text{Sr}/^{86}\text{Sr}$,
326 $^{143}\text{Nd}/^{144}\text{Nd}$ and lower $^{206}\text{Pb}/^{204}\text{Pb}$ (< 18) (Zhang et al., 2018). Therefore, it is unlikely
327 to be the source of the SE Asian (including the SCS seamount) volcanism.

328 Subducting marine sediment, seawater-altered ocean crust and EMII have similar
329 Pb isotope compositions but can extend to more radiogenic $^{87}\text{Sr}/^{86}\text{Sr}$ and could serve
330 as this end member (**Fig. 6**). Compared to matrix glass, plag-hosted melt inclusions
331 extend to lower (Ce, Nd)/Pb but higher Ba/La ratios (**Table S2**), also favoring
332 sediments as the EMII component. Geophysical studies provide additional support for

333 recycled oceanic crust components beneath the SCS and Indochina. They could
334 originate from subducted Neo-Tethyan slabs from the southwest (230 – 90 Ma)
335 (Chung et al., 2005), or paleo-Pacific and Pacific slabs from the east (300 – 120 Ma)
336 (Li and Li, 2007). Given that the SE China region was far from the Neo-Tethyan
337 tectonic realm during the Mesozoic, it is likely that recycled Neo-Tethyan slabs are
338 not the major source of the FOZO-like signature observed in Cenozoic lavas.

339 The observed Sr and Pb isotopic heterogeneity in young (130-170 Ma) Pacific
340 oceanic crust and marine sediments from ODP sites 801 and 1149, east of the Mariana
341 and Izu-Bonin arcs (Hauff et al., 2003), respectively, covers the entire range exhibited
342 by SCS spreading MORB, post-spreading volcanism and their crystal cargoes and
343 melt inclusions, and even extends to more extreme compositions (**Fig. 6**). For the
344 purpose of our modelling, we considered Pacific MORB from site 801C with high μ
345 ($^{238}\text{U}/^{204}\text{Pb} = 51$) and radiogenic Pb ($^{206}\text{Pb}/^{204}\text{Pb} = 20.03$; $^{207}\text{Pb}/^{206}\text{Pb} = 0.777$;
346 $^{208}\text{Pb}/^{206}\text{Pb} = 1.881$; Hauff et al., 2003) as the FOZO component (Hanan and Graham,
347 1996; Stracke et al., 2005). Marine sediments (clay, chert and nannofossil marl) from
348 Sites 801 and 1149 in Pacific Ocean with very radiogenic Sr ($^{87}\text{Sr}/^{86}\text{Sr} = 0.70954$) and
349 relatively radiogenic Pb ($^{206}\text{Pb}/^{204}\text{Pb} = 18.61$, $^{207}\text{Pb}/^{206}\text{Pb} = 0.845$, and $^{208}\text{Pb}/^{206}\text{Pb} =$
350 2.089) (Hauff et al., 2003) as the EMII component. Our isotope modeling results (**Fig.**
351 **5 and 6**) show that the isotopic heterogeneity seen in the SCS spreading- and
352 post-spreading lavas could represent mixtures of depleted upper mantle with recycled
353 oceanic crust and sediment.

354 The FOZO component ubiquitous in mid-ocean-ridge and intraplate basalts was
355 proposed to represent young ocean crust recycled through the transition zone and/or
356 upper mantle (Hanan and Graham, 1996; Stracke et al., 2005). Since the SCS lavas
357 have $^3\text{He}/^4\text{He}$ ($7.4 - 8.0 R/R_A$) similar to or lower than MORB (Qian et al., 2021), the
358 MTZ is the most likely storage location for ocean crust evolving to FOZO (Hanan and
359 Graham, 1996). Here we use a Monte Carlo simulation (see **Fig. 7, S7, and Table**
360 **S11**; see supplementary material for further details) to constrain the possible
361 combinations of source maturation times (in Ma) and μ ($^{238}\text{U}/^{204}\text{Pb}$) values required to
362 reproduce the FOZO-like Pb isotope signature seen in the SCS. The Monte Carlo
363 simulation (**Fig. 7, S7 and Table S11**) randomly chooses an initial Pb isotope
364 compositions and a μ value, which falls within the range seen in typical unradiogenic
365 paleo-Pacific oceanic crust, then calculates the time required to evolve to the FOZO
366 endmember. Pb isotope compositions always take longer to evolve with a lower μ , but
367 all scenarios are consistent with the relatively short timescales (< 500 Myr) needed to
368 generate the required FOZO-like isotope signature (**Fig. 7**). Based on the average μ of
369 42 measured in Pacific oceanic crust all the potential initial compositions can
370 reproduce the FOZO-like component in less than 120 – 350 Myr (**Fig. 7**). Thus, on the
371 basis of the unique geochemical constraints and geological setting, it seems most
372 plausible that the MTZ beneath SE Asia was most likely enriched by subducted
373 materials from past paleo-Pacific plate subduction. Given that the subduction of the
374 paleo-Pacific plate beneath SE Asia took place between c. 250 and 150 Ma (Li and Li,

375 2007), the timescales for oceanic crust recycling in marginal sea basin (e.g., < c. 250
376 Ma) are significantly shorter than those associated with the plate deep subduction and
377 mantle plume upwelling (possibly > 1.0 Gyr) (Chase, 1981; Hanyu et al., 2019;
378 Stracke et al., 2003). It has previously been shown that the Pb isotopic composition of
379 FOZO can be generated from 300 Ma-age oceanic crust, if some Pb from a
380 continental source (e.g. pelagic sediments) was added during hydrothermal alteration
381 shortly after crust formation (Hanan and Graham, 1996). In particular, given that the
382 abundant seamount lavas or OIBs formed during the seafloor spreading and
383 post-spreading stage are highly variable in isotopic composition, their subduction and
384 recycling could be a plausible process to produce enriched MORB or intraplate lavas
385 isotopic signatures over relatively short timescales. The MTZ has been proposed as
386 the most likely storage location for such young ocean crust evolving to these
387 FOZO-like intermediate compositions (Hanan and Graham, 1996; Stracke et al.,
388 2005). Thus, recycling of ocean crust through the upper mantle and transition zone
389 can occur on relatively short time scales. This rapid reworking is consistent with other
390 studies that have argued for short (≤ 600 Myr) recycling times based on evidence
391 from mid-ocean ridge and intraplate volcanism (e.g. Hoernle et al., 2011; Mazza et
392 al., 2019; McCoy-West et al., 2016; Sobolev et al., 2011). Ultimately, recycling of
393 enriched oceanic lithosphere through the transition zone over those short time scales
394 (< 250 Myr) seen in the SCS has the potential to significantly enhance upper mantle
395 heterogeneity.

396

397 *5.3 Source heterogeneity and melting process control on geochemical variations of*
398 *late Cenozoic volcanism*

399 Our new Ar-Ar dating results show that the Shixingbei seamount is 19.10 ± 0.78
400 Ma (**Fig. 2A**), and is 3 – 5 Myr younger than the underlying MORBs, which formed
401 around 23 – 24 Ma with a spreading rate of c. 25 km/Myr based on magnetic anomaly
402 data (Li et al., 2014). The final age of seafloor spreading in the ESB of the SCS is
403 estimated to be c. 15 Ma (Li et al., 2014). The Shixingbei seamount, is ≤ 150 km
404 away from the present-day fossil ridge axis in the ESB (**Fig. 1**), indicating that it
405 formed off-axis on the flank of the fossil ridge.

406 Off-axis seamounts can form near a ridge axis if an excessive magma supply is
407 available from residual mantle upwelling feeding volcanic activity on the ridge axis.
408 Following abandonment of a spreading ridge, the average degree of mantle melting
409 under the abandoned ridge progressively decreases with time due to the decrease in
410 mantle upwelling rate (seafloor spreading rate) and the increase in overlying
411 lithosphere thickness by conductive cooling as it moves further off-axis (Brandl et al.,
412 2012; Haase et al., 2011). This is observed in the off-axis Shixingbei seamount where
413 the seafloor spreading rate in the SCS decreased rapidly due to a ridge jump at 25 Ma
414 (Li et al., 2014). As off-axis seamount lavas are generated by lower degrees of
415 melting of heterogeneous mantle they would contain a larger contribution from more
416 fusible and enriched components, which are expected to have relatively enriched

417 geochemical flavor (e.g., Brandl et al., 2012; Castillo et al., 2010; Haase et al., 2011).
418 Compared to the SCS spreading stage MORBs, the off-axis Shixingbei seamount
419 basalts have more enriched trace element (elevated La/Sm and Nb/Zr, **Fig. 4**) and
420 isotopic compositions (more radiogenic Sr and less radiogenic Nd isotope signatures,
421 **Fig. 5**). Thus, the off-axis Shixingbei seamounts lavas were generated by lower
422 degrees of melting of a heterogeneous magma source relative to SCS MORBs
423 generated at the spreading center.

424 The Zhengbei and Huangyan seamounts have been dated at c. 7.8 Ma (**Fig. 2**),
425 which is much younger than the underlying fossil spreading ridge in the ESB of the
426 SCS that was active at 15 Ma (Li et al., 2014). Previous studies have shown that
427 buoyancy-induced upwelling by melt-depleted residual mantle and associated lower
428 degree melting relative to spreading stage can be responsible for continued
429 magmatism on fossil ridges for several Myr after active spreading ceased (Brandl et
430 al., 2012; Castillo et al., 2010; Haase et al., 2011). A similar mechanism can explain
431 to some extent the enriched geochemical signatures observed in some seamounts on
432 the SCS fossil ridges that erupted several Myr after spreading ceased. The
433 post-spreading stage Huangyan and Zhenbei seamount lavas are characterized by
434 E-MORB- to OIB-type incompatible element abundances, and compared to the
435 spreading stage MORBs and off-axis Shixingbei seamount lavas, show a significantly
436 higher La/Sm, fractionated HREE element patterns ($\text{Sm/Yb} \gg 1$), and more enriched
437 Sr and Nd isotope compositions (**Fig. 4, 5**). This suggests that the post-spreading

438 seamount lavas were most likely generated by lower degrees of melting with residual
439 garnet in their mantle source. The geochemical compositions of SCS seamount lavas
440 together with the new age data indicate that the variable degrees of melting of
441 heterogeneous mantle can reproduce the trace element and isotope variations in the
442 lavas.

443 Interestingly, similar features are observed in intraplate volcanism throughout SE
444 Asia, there is a large contrast in the compositions of magma generated during the SCS
445 spreading (33 – 16 Ma) and post-spreading (post-16 Ma) stages (**Fig. 4, 5, 8C and D**).
446 Spatially, compared to the post-spreading seamount lavas in the SCS basin, there are
447 significantly larger chemical and isotopic variations (e.g., Sm/Yb and $^{87}\text{Sr}/^{86}\text{Sr}$) in the
448 intraplate basalts from neighboring areas (western- and northern-group), although this
449 could simply reflect much less data from the SCS basin (**Fig. 8E, F**). The
450 post-spreading basalts in the SCS basin erupted on thinner lithosphere (45 – 50 km)
451 have geochemical characteristics consistent with higher degrees (F) and shallower
452 depths (P) of melting (e.g., lower Sm/Yb; **Fig. 8E**), whereas intraplate basalts erupted
453 on thicker lithosphere (60 – 90 km) (Wu et al., 2004) (e.g., south China and
454 Indochina, north and west of the SCS) show the inverse (**Fig. 8E**). In accordance with
455 these observations, we propose that there was a common mantle source beneath SE
456 Asia during the spreading and post-spreading stages, but the enriched (OIB-type)
457 mantle was generally more diluted in the SCS MORBs and seamount lavas due to
458 greater degrees of melting at shallower depths. Our new results support a model

459 where variable degrees of melting of a heterogeneous mantle are responsible for
460 geochemical variability of MORBs and OIBs (Meibom and Anderson, 2004).

461

462 *5.4 Volcanism in SE Asia linked to subduction-induced mantle upwelling*

463 The cause of intraplate volcanism and dynamics of mantle upwelling in SE Asia
464 are subject to debate, and have been variously attributed to the Hainan mantle plume
465 (e.g. Wang et al., 2013; Yan et al., 2018; Zou & Fan, 2010), plate subduction induced
466 mantle flow (e.g. Lin et al., 2019; Qian et al., 2021), and eastward mantle flow escape
467 in response to Indo-Eurasian collision (e.g., Hoang & Flower, 1998). The volcanism
468 in SE Asia is not easily explained by the model of a mantle plume rooted at the core–
469 mantle boundary under Hainan island because: (1) multiple volcanic episodes of
470 distinct chemistry and age are observed in SE Asia (Hoang and Flower, 1998; **Fig. 1**);
471 (2) the volcanism around Hainan island is much younger and obviously weaker than
472 that in nearby areas (SE China, SCS and Indochina) (**Fig. 1**); (3) $^3\text{He}/^4\text{He}$ of SCS
473 seamount glasses (7.36 to 8.03 R/R_A) are significantly lower than classical mantle
474 plume-derived basalts (Hawaii and Iceland) but typical of normal MORB (Qian et al.,
475 2021); (4) there is no well-defined ‘hotspot’ track associated with age-progressive
476 volcanism in SE Asia (Li et al., 2014; this study); and, (5) broad (i.e. non
477 plume-shaped), ambiguous P-wave tomographic anomalies above the transition zone
478 together with weaker, diminishing slow anomalies below the transition zone beneath

479 SE Asia, challenge the view of the ‘Hainan plume’ as a classical plume structure (Lin
480 et al., 2019).

481 The SE Asia region is surrounded by several sub-duction zones (**Fig. 1**),
482 suggesting a potential association between plate subduction and magmatic activity
483 (Lin et al., 2019). During the seafloor spreading stage of the SCS, in addition to
484 formation of new oceanic crust and a small number of seamounts near the spreading
485 center, igneous activity (with ages between 26 – 16 Ma) occurred predominantly
486 along coastal SE China and the SCS northern margin (see **Fig. 1, 8A**). Its spatial
487 extent could indicate that the spreading stage volcanism might be induced by
488 westward subduction of the Pacific and Philippine Sea plates beneath Eurasia, since
489 these were located along eastern SE Asia. Intraplate magmatism within Indochina
490 (peaking < 8 Ma) is generally younger than along coastal SE China (generally 10 – 16
491 Ma) (Hoang and Flower, 1998; **Fig. 1, 8A and B**). Seismic tomography studies show
492 evidence for the subduction of the Indo-Australian plate beneath SE Asia along the
493 Sunda trench with slab segments deflected horizontally in the MTZ towards the SCS
494 and Indochina (Li and van der Hilst, 2010). Therefore, it seems likely that Cenozoic
495 volcanism in Indochina could be related to subduction-induced mantle upwelling
496 along the Sunda trench. Hainan island is far from any subduction zones and shows
497 intraplate volcanism peaking < 5 Ma, much younger than the age of the volcanism in
498 the SCS and coastal areas of SE China (Zou and Fan, 2010; **Fig. 1, 8B**). Thus, the
499 spatiotemporal distribution and evolution of the intraplate volcanism could plausibly

500 be active upwelling of mantle material linked to circular subduction systems of the
501 Pacific, Philippine Sea, and Indo-Australian plates (**Fig. 9**). Indeed, geodynamic
502 models that tested a variety of input SE Asian plate reconstructions demonstrated
503 robust, localized upper mantle upwellings within SE Asia during the Cenozoic that
504 were induced by the regional subduction (Lin et al., 2019).

505 Here, we propose a simple conceptual model linking the flux from multiple
506 subducting plates to upper mantle heterogeneity, and volcanism in SE Asia (**Fig. 9**).
507 The induced mantle upwelling associated with local subduction can be generated
508 ahead of a deep subducting slab and adjacent to edges of the stagnant slab segments in
509 the transition zone, despite being far from arcs (Faccenna, 2010). Recent geodynamic
510 models showed that this slab flux would stimulate upwelling of the enriched MTZ
511 reservoirs and eventually lead to volcanic eruptions (Mather et al., 2020). We suggest
512 that this subduction-induced upwelling originating from the MTZ and surrounding
513 area as revealed by seismic tomography, and associated decompression melting feed
514 the diffuse and non-age-progressive volcanism in SE Asia. A similar mantle return
515 flow, driven by long-lived subduction, has also been proposed to cause the intraplate
516 volcanism across eastern Australia and Zealandia, as well as northern and
517 northeastern China (Mather et al., 2020; Zhao et al., 2011). Slab-triggered mantle
518 return flow beneath SE Asia is significantly more complex than under eastern
519 Australia-Zealandia and, northern and northeastern China, as SE Asia is surrounded
520 by complicated convergent subduction systems on three sides. Therefore, it remains

521 challenging at present to reconstruct and pinpoint the exact geochemical signature and
522 mantle flows associated with a specific subducted slab flux. Further geodynamic
523 modeling, high-resolution seismological studies and geochemical and age constraints
524 on magmatism are required to quantify the link between cycling of
525 subduction-induced mantle flows and time-space evolution of volcanism.

526

527 **6. Conclusions**

528 We present new geochemical and geochronological data for lavas from the
529 South China Sea (SCS) seamounts. Through comparison with existing geochemical
530 data we investigate mantle source compositions and the mantle evolution, and infer a
531 possible mechanism to generate mantle heterogeneity and the volcanism in the SCS
532 and surrounding areas. The major results of this work are as follows:

533 1. The Shixingbei seamount lavas formed during the syn-spreading stage (19.1
534 Ma; 33–16 Ma) are limited to tholeiitic basalts. The Zhenbei-Huangyan seamount
535 lavas formed during the post-spreading stage (7.8 Ma) show wide variations in
536 chemical compositions, ranging from basanite through alkali basalt to trachyte. The
537 SCS Shixingbei seamount tholeiitic basalts are more depleted in incompatible trace
538 element (e.g. La/Sm and Sm/Yb), and have less radiogenic $^{87}\text{Sr}/^{86}\text{Sr}$ and more
539 radiogenic $^{143}\text{Nd}/^{144}\text{Nd}$ relative to most post-spreading lavas. Mantle source
540 heterogeneity together with melting process control spatial–temporal (spreading and

541 post-spreading stage) geochemical variations of lavas from the SCS and surrounding
542 areas.

543 2. Zhenbei-Huangyan seamount whole rocks, matrix glass and plag show
544 limited isotopic variation, while ol-hosted and plag-hosted melt inclusions show large
545 variations in radiogenic Sr and Pb isotope ratios. A three-component mixing model
546 (DMM-EMII-FOZO) is required to adequately explain the variability in isotopic
547 compositions of the ol-hosted and plag-hosted melt inclusions.

548 3. The combined trace element and isotopic data of the SCS seamount melt
549 inclusions, minerals and lavas demonstrate that the mantle source in the region is
550 influenced by a package of young recycled oceanic crust with variable amounts of
551 sediment. Combined with geophysical evidence, this demonstrates that recycling of
552 ocean crust and marine sediments through the upper mantle from the MTZ can occur
553 on relatively short time scales (< 250 Myr), much faster than those associated with the
554 plate deep subduction and mantle plume upwelling (possibly > 1 Gyr). This new
555 evidence shows that the production of mantle reservoirs enriched by the storage of
556 past subducted slabs in the mantle transition zone is an important mechanism in the
557 generation of distinctive isotopic domains that were generally thought to be related to
558 deep recycling.

559 4. Our results show that marginal basins are important sites for introducing
560 enriched oceanic and continental lithospheric material, i.e., chemical heterogeneity,
561 into the upper mantle and transition zone. Subduction-induced upwelling from the

562 mantle transition zone and nearby areas can explain the late Cenozoic volcanism
563 observed in SE Asia.

564

565 **Acknowledgements**

566 We are grateful for the very constructive reviews by two anonymous reviewers,
567 and for the very useful suggestion by the editor Rosemary Hickey-Vargas, that all
568 helped greatly to clarify several points in our manuscript. We are very grateful to Kaj
569 Hoernle, Jenna V. Adams, Zhongyuan Ren, Yigang Xu, Guoliang Zhang and
570 Matthew G. Jackson for helpful discussions. We thank Anthony A. P. Koppers,
571 Daniel P. Miggins, Lingmin Zhang and Hao Cheng for assistance in the sample
572 analysis. This study was supported by the National Natural Science Foundation (NSF)
573 of China (41902044 and 91428207). Jonny Wu was supported by US NSF grant
574 EAR- 1848327. AMW was supported by ARC grant DE210101395.

575

576

577 **Figure captions**

578 **Fig. 1.** Simplified geological map of the South China Sea (SCS) and adjacent regions,
579 and sampling locations. (A) Bathymetric map of the present-day SCS and adjacent
580 regions. Distribution of late Cenozoic intraplate volcanism in the SCS basin (red
581 circles) and surrounding area (e.g., western group including Indochina block and
582 Hainan (grey circles); and northern group including Southeast China and Taiwan

583 (blue circles)) are shown with ages labeled in red. Spreading stage volcanism (pink
584 dots) is also shown with ages labeled in black (Age data for both are from the
585 GEOROC database (<http://georoc.mpchmainz.gwdg.de/georoc>)). Major magnetic
586 anomalies (blue lines) are also shown and marked with anomaly numbers after Li et
587 al. (2014). The red dashed lines show the final fossil ridges and the pink dashed line
588 marks the location of the ridge jump with the arrow indicating the direction of ridge
589 migration. Bathymetric data were taken from GEBCO_2014 Grid
590 (<http://www.gebco.net>). SXB, Shixingbei; ZB, Zhenbei; HY, Huangyan. ESB, East
591 Sub-basin; SWSB, Southwest Sub-basin; NWSB, Northwest Sub-basin. (B) The
592 major subduction zones surrounding the SCS and the Indochina Peninsula. Inset map
593 showing location of tomographic profile (A1-A2) presented in Fig. 9.

594

595 **Fig. 2.** The ages of the South China Sea seamount lava samples. (A-B) $^{40}\text{Ar}/^{39}\text{Ar}$ age
596 spectrum for plagioclase from the Shixingbei and Huangyan seamount lavas. (C)
597 U-Pb zircon concordia plot for sample 2059-R16 from Zhebei seamount. Inset is the
598 weighted average of zircon $^{206}\text{Pb}/^{238}\text{U}$ ages.

599

600 **Fig. 3.** Variation of major elements in whole rocks, melt inclusions and matrix glasses
601 for South China Sea (SCS) seamount lavas. (A) SiO_2 versus (vs.) total alkali
602 ($\text{Na}_2\text{O}+\text{K}_2\text{O}$) content, MgO vs. (B) FeO^t , (C) Al_2O_3 , and (D) CaO for whole rocks
603 (WR), matrix glasses (mgl), and olivine (ol)-hosted and plagioclase (plag)-hosted melt

604 inclusions (MI) from Shixingbei, Huangyan and Zhenbei seamounts. Data of
605 spreading stage MORB and post-spreading lavas in the SCS and intraplate volcanism
606 in surrounding area (e.g. Southeast China, Taiwan and Indochina) are from the
607 GEOROC (<http://georoc.mpchmainz.gwdg.de/georoc>). Mineral abbreviations cpx and
608 ilm denote clinopyroxene and ilmenite, respectively.

609

610 **Fig. 4.** Variation of trace elements in whole rocks, melt inclusions and matrix glasses
611 for South China Sea (SCS) seamount lavas. (A-B) Incompatible multi-element
612 diagrams, (C) Nb/Zr vs. La/Sm, (D) Sm/Yb vs. La/Sm for whole rocks (WR) from
613 Shixingbei, Huangyan and Zhenbei seamounts, and matrix glass and melt inclusion
614 from Huangyan lavas. Trace element data of primitive mantle, N-MORB, E-MORB
615 and OIB are from Sun and McDonough (1989). The SCS spreading stage MORBs
616 (Zhang et al., 2018), and Pacific and Indian MORBs (Gale et al., 2013) are shown for
617 comparisons. Data source of intraplate volcanism in southeast (SE) Asia is the same
618 as in Fig. 3. To minimize the effect of crustal contamination, intraplate lavas in SE
619 Asia with $\epsilon_{Nd} < 2.7$ have been excluded.

620

621 **Fig. 5.** Geochemical characteristics of the South China Sea (SCS) seamount samples.
622 (A) $^{87}\text{Sr}/^{86}\text{Sr}$ vs. $^{143}\text{Nd}/^{143}\text{Nd}$, (B) $^{143}\text{Nd}/^{143}\text{Nd}$ vs. $^{206}\text{Pb}/^{204}\text{Pb}$, (C) $^{87}\text{Sr}/^{86}\text{Sr}$ vs.
623 $^{206}\text{Pb}/^{204}\text{Pb}$, (D) $^{207}\text{Pb}/^{204}\text{Pb}$ vs. $^{206}\text{Pb}/^{204}\text{Pb}$ for whole rocks (WR) from Shixingbei,
624 Huangyan and Zhenbei seamounts. Data sources: the SCS spreading stage MORBs

625 (Zhang et al., 2018); Pacific MORBs, EMI-type and EMII-type oceanic island basalts
626 (Stracke et al., 2003), and intraplate lavas in the SCS and SE Asia from the GEOROC
627 database (<http://georoc.mpchmainz.gwdg.de/georoc>). The modeling results show
628 mixing trends (solid lines) between depleted SCS MORB mantle end-component
629 (DMM) and recycled oceanic crust and sediments. Dashed lines show mixing between
630 averaged Pacific MORB, and typical EMII mantle derived partial melt. To minimize
631 the effect of crustal contamination, intraplate lavas in southeast Asia with $\epsilon_{Nd} < 2.7$
632 have been excluded. The main parameters in the mixing model are given in
633 Supplementary Table S9.

634

635 **Fig. 6.** Isotopic variations in melt inclusions, whole rocks and matrix glasses for
636 South China Sea (SCS) seamount lavas. (A) $^{87}\text{Sr}/^{86}\text{Sr}$ vs. $^{207}\text{Pb}/^{206}\text{Pb}$ and (B)
637 $^{207}\text{Pb}/^{206}\text{Pb}$ vs. $^{208}\text{Pb}/^{206}\text{Pb}$ isotope diagram for whole rocks from Shixingbei seamount
638 lavas, and whole rocks (WR), matrix glass (mgl), olivine (ol)-hosted and plagioclase
639 (plag)-hosted melt inclusions (MI) and feldspars from Huangyan and Zhenbei
640 seamount lavas, illustrating that at least three components are required to explain the
641 observed variations in isotopic composition: DMM-depleted SCS MORB-source
642 upper mantle, represented by the most depleted SCS MORB (Zhang et al., 2018),
643 FOZO-type component, interpreted as reflecting the young recycled material in the
644 mantle transition zone (Hanan and Graham, 1996; Stracke et al., 2005), well
645 represented by young recycled Mesozoic Pacific MORB (Hauff et al., 2003), and an

646 EMII-type component – represented by Mesozoic Pacific Ocean sediment (Hauff et
647 al., 2003). The main parameters in the three-component-mixing model between DMM
648 and recycled oceanic crust and sediments are the same as in Fig. 5. Data sources:
649 unpublished data from olivine-hosted melt inclusions from Hainan island lavas, to the
650 north of the SCS, from Ren (personal communication 2021); the SCS post-spreading
651 lavas, and Pacific and Indian MORB (<http://georoc.mpch-mainz.gwdg.de/georoc/>);
652 U1431 SCS spreading stage MORBs (Zhang et al., 2018); Mesozoic Pacific ocean
653 crust (Hauff et al., 2003); EMII (typical EM-2 OIBs), and HIMU (typical HIMU
654 OIBs) end members (Stracke et al., 2003); FOZO (Stracke et al., 2005) and C (Hanan
655 and Graham, 1996). To minimize the effect of crustal contamination, intraplate lavas
656 in southeast Asia with $\epsilon_{Nd} < 2.7$ have been excluded.

657

658 **Fig. 7.** Results of Monte Carlo simulations for Pb model evolution of the recycled
659 component in FOZO mantle source. (A) Monte Carlo results derived from Equation
660 (1) in the supplementary material for R1 values. $\mu = {}^{238}\text{U}/{}^{204}\text{Pb}$, the green area shows
661 the range for μ values for Pacific oceanic crust and the dashed blue line defines the
662 average μ value; (B) Modelling μ in the mantle source. Modelled μ compositions that
663 are necessary to produce radiogenic ${}^{206}\text{Pb}/{}^{204}\text{Pb}$ of typical FOZO (${}^{206}\text{Pb}/{}^{204}\text{Pb} = 20.03$)
664 signature starting from an un-radiogenic sample (${}^{206}\text{Pb}/{}^{204}\text{Pb} = 18.5$) of the
665 paleo-Pacific oceanic crust (Hauff et al., 2003). Each line corresponds to possible

666 source ages and the necessary μ for that source to generate the radiogenic $^{206}\text{Pb}/^{204}\text{Pb}$
667 of typical FOZO lavas.

668

669 **Fig. 8.** Spatial and temporal evolution of Cenozoic lavas in the South China Sea
670 (SCS) and surrounding areas. (A-B) Histogram showing age ranges for Cenozoic
671 (spreading- and post-spreading stage) lavas in the SCS and surrounding areas. (C-D)
672 Temporal variation of geochemical composition of spreading- and post-spreading
673 stage lavas in the SCS and surrounding areas. (E-F) Spatial variation of geochemical
674 composition of intraplate lavas from the SCS, western group (Indochina and
675 Leiqiong, to the west of the SCS) and northern group (including south China and
676 Taiwan, to the north of the SCS) shown in Fig. 1. Data for ages and compositions of
677 Cenozoic lavas in the Southeast Asia from the GEOROC
678 (<http://georoc.mpchmainz.gwdg.de/georoc>). Intraplate lavas in southeast Asia affected
679 by crustal contamination have been excluded.

680

681 **Fig. 9.** Schematic model illustrating the formation mechanism of the Cenozoic
682 volcanism in southeast Asia based on integration of seismic and geochemical data.
683 Mantle structure beneath the SCS shown by FWEA18 full waveform tomography
684 P-wave perturbations (Tao et al., 2018) and earthquakes (red circles). Tomographic
685 fast anomalies indicate a swath of sub-horizontal subducted oceanic lithosphere
686 beneath the SCS at 500 – 700 km depths from previous subduction events. Although a

687 small amount of stagnant material may be older recycled slabs from past subduction,
688 most of the visible stagnant slab segments stored in the transition zone imaged by
689 seismic tomography are likely to be younger subducted slabs from nearby
690 circum-SCS subduction zones (i.e. Indo-Australian, Pacific, Philippine Sea plates, or
691 Proto-SCS slabs). Even after SCS spreading ceased at 15 Ma, the more buoyant
692 metasomatized mantle continues to upwell and melt to form the SCS seamounts and
693 possibly intraplate basalts in South China and Indochina with EMII type
694 compositions.

695

696 **References**

- 697 Brandl, P.A., Beier, C., Regelous, M., Abouchami, W., Haase, K.M.,
698 Garbe-Schönberg, D., Galer, S.J.G., 2012. Volcanism on the flanks of the East
699 Pacific Rise: quantitative constraints on mantle heterogeneity and melting
700 processes. *Chemical Geology* 289-299, 41-56.
- 701 Briais, A., Patriat, P., Tapponnier, P., 1993. Updated interpretation of magnetic
702 anomalies and seafloor spreading stages in South China Sea: implications for the
703 Tertiary tectonics of Southeast Asia. *J. Geophys. Res.* 98, 6299–6328.
- 704 Castillo, P. R., Clague, D. A., Davis, A. S., Lonsdale, P. F., 2010. Petrogenesis of
705 Davidson Seamount lavas and its implications for fossil spreading center and
706 intraplate magmatism in the eastern Pacific. *Geochem. Geophys. Geosyst.* 11.

707 Chase, C.G., 1981. Oceanic island Pb: two-stage histories and mantle evolution. *Earth*
708 *Planet Sc Lett* 52, 277–284.

709 Chung, S.-L., Chu, M.-F., Zhang, Y., Xie, Y., Lo, C.-H., Lee, T.-Y., Lan, C.-Y., Li,
710 X., Zhang, Q., Wang, Y., 2005. Tibetan tectonic evolution inferred from spatial
711 and temporal variations in post-collisional magmatism. *Earth-Sci Rev* 68,
712 173-196.

713 Faccenna, C., Becker T.W., Lallemand, S., Lagabrielle, Y., Funiciello, F., Piromallo,
714 Claudia., 2010. Subduction-triggered magmatic pulses: A new class of plumes?
715 *Earth Planet Sc Lett* 299, 54–68.

716 Gale, A., Dalton, C.A., Langmuir, C.H., Su, Y.J., Schilling, J.G., 2013. The mean
717 composition of ocean ridge basalts. *Geochem Geophys Geosy* 14, 489-518.

718 Haase, K.M., Regelous, M., Duncan, R.A., Brandl, P.A., Stroncik, N., Grevemeyer, I.,
719 2011. Insights into mantle composition and mantle melting beneath mid-ocean
720 ridges from post-spreading volcanism on the fossil Galapagos Rise. *Geochem.*
721 *Geophys. Geosyst.* 12, Q0AC11.

722 Hanan, B.B., Graham, D.W., 1996. Lead and Helium Isotope Evidence from Oceanic
723 Basalts for a Common Deep Source of Mantle Plumes. *Science* 272, 991-995.

724 Hanyu, T., Shimizu, K., Ushikubo, T., Kimura, J.-I., Chang, Q., Hamada, M., Ito, M.,
725 Iwamori, H., Ishikawa, T., 2019. Tiny droplets of ocean island basalts unveil
726 Earth's deep chlorine cycle. *Nat Commun* 10, 60.

727 Hauff, F., Hoernle, K., Schmidt, A., 2003. Sr-Nd-Pb composition of Mesozoic Pacific
728 oceanic crust (Site 1149 and 801, ODP Leg 185): Implications for alteration of
729 ocean crust and the input into the Izu-Bonin-Mariana subduction system.
730 *Geochem Geophys Geosyst* 4.

731 Hickey-Vargas, R., 1992. A refractory HIMU component in the sources of island arc
732 magma, *Nature* 360, 57-59.

733 Hoang, N., Flower, M., 1998. Petrogenesis of Cenozoic basalts from Vietnam:
734 implication for origins of a 'Diffuse Igneous Province'. *J. Petrol.* 39, 369-395.

735 Hoernle, K., Hauff, F., Werner, R., van den Bogaard, P., Gibbons, A.D., Conrad, S.,
736 Müller, R.D., 2011. Origin of Indian Ocean Seamount Province by shallow
737 recycling of continental lithosphere. *Nat Geosci* 4, 883.

738 Höfig, T.W., Geldmacher, J., Hoernle, K., Hauff, F., Duggen, S., Garbe-Schönberg,
739 D., 2014. From the lavas to the gabbros: 1.25km of geochemical characterization
740 of upper oceanic crust at ODP/IODP Site 1256, eastern equatorial Pacific. *Lithos*
741 210-211, 289-312.

742 Hofmann, A.W., 1997. Mantle geochemistry: The message from oceanic volcanism.
743 *Nature* 385, 219-229.

744 Jackson, M.G., Hart, S.R., 2006. Strontium isotopes in melt inclusions from Samoan
745 basalts: Implications for heterogeneity in the Samoan plume. *Earth Planet Sc Lett*
746 245, 260-277.

747 Kamenetsky, V.S., Crawford, A.J., Eggins, S., Muhe, R., 1997. Phenocryst and melt
748 inclusion chemistry of near-axis seamounts, Valu Fa Ridge, Lau Basin: insight
749 into mantle wedge melting and the addition of subduction components. *Earth
750 Planet Sc Lett* 151, 205-223.

751 Kent, A.J.R., 2008. Melt Inclusions in Basaltic and Related Volcanic Rocks. *Rev
752 Mineral Geochem* 69, 273-331.

753 Li, C.-F., Xu, X., Lin, J., Sun, Z., Zhu, J., Yao, Y., Zhao, X., Liu, Q., Kulhanek, D.K.,
754 Wang, J., Song, T., Zhao, J., Qiu, N., Guan, Y., Zhou, Z., Williams, T., Bao, R.,
755 Briais, A., Brown, E.A., Chen, Y., Clift, P.D., Colwell, F.S., Dadd, K.A., Ding,
756 W., Almeida, I.H., Huang, X.-L., Hyun, S., Jiang, T., Koppers, A.A.P., Li, Q.,
757 Liu, C., Liu, Z., Nagai, R.H., Peleo-Alampay, A., Su, X., Tejada, M.L.G., Trinh,
758 H.S., Yeh, Y.-C., Zhang, C., Zhang, F., Zhang, G.-L., 2014. Ages and magnetic
759 structures of the South China Sea constrained by deep tow magnetic surveys and
760 IODP Expedition 349. *Geochem Geophys Geosy* 15, 4958-4983.

761 Li C., van der Hilst, R.D., 2010. Structure of the upper mantle and transition zone
762 beneath Southeast Asia from traveltimes tomography, *J. Geophys. Res.* 115,
763 B07308.

764 Li, Z.-X., Li, X.-H., 2007. Formation of the 1300-km-wide intracontinental orogen
765 and postorogenic magmatic province in Mesozoic South China: a flat-slab
766 subduction model. *Geology* 35, 179-182.

767 Lin, J., Xu, Y.G., Sun, Z., Zhou, Z.Y., 2019. Mantle upwelling beneath the South
768 China Sea and links to surrounding subduction systems. *Natl. Sci. Rev.* 6 (5),
769 877–881.

770 Mather, B.R., Müller, R.D., Seton, M., Ruttor, S., Nebel, O., Mortimer, N., 2020.
771 Intraplate volcanism triggered by bursts in slab flux. *Sci. Adv.* 6(51), eabd0953.

772 Mazza, S.E., Gazel, E., Bizimis, M., Moucha, R., Béguelin, P., Johnson, E.A.,
773 McAleer, R.J., Sobolev, A.V., 2019. Sampling the volatile-rich transition zone
774 beneath Bermuda. *Nature* 569, 398.

775 McCoy-West, A.J., Bennett, V.C., Amelin, Y., 2016. Rapid Cenozoic ingrowth of
776 isotopic signatures simulating “HIMU” in ancient lithospheric mantle:
777 Distinguishing source from process. *Geochim Cosmochim Acta* 187, 79-101.

778 Meibom, A., Anderson, D.L., 2004. The statistical upper mantle assemblage. *Earth
779 Planet Sc Lett* 217, 123-139.

780 Peate, D.W., Peate, I.U., Rowe, M.C., Thompson, J.M., Kerr, A.C., 2012.
781 Petrogenesis of High-MgO Lavas of the Lower Mull Plateau Group, Scotland:
782 Insights from Melt Inclusions. *J Petrol* 53, 1867-1886.

783 Qian, S., Gazel, E., Nichols, A. R. L., Cheng, H., Zhang, L., Salters, V. J., Li, J., Xia,
784 X.P., Zhou, H.Y., 2021. The origin of late Cenozoic magmatism in the South
785 China Sea and Southeast Asia. *Geochem Geophys Geosy* 22.

786 Qian, S.P., Ren, Z.Y., Richard, W., Zhang, L., Zhang, Y.H., Hong, L.B., Ding, X.L.,
787 Wu, Y.D., 2017. Petrogenesis of Early Cretaceous basaltic lavas from the North

788 China Craton: Implications for cratonic destruction. *J. Geophys. Res.*, 122,
789 1900-1918.

790 Ramos, F., Tepley Iii, F., 2008. Inter- and Intracrystalline Isotopic Disequilibria:
791 Techniques and Applications. *Rev Mineral Geochem* 69.

792 Rose-Koga, E., Koga, K., Moreira, M., Vlastélic, I., Jackson, M., Whitehouse, M.J.,
793 Shimizu, N., Habib, N., 2017. Geochemical systematics of Pb isotopes, fluorine,
794 and sulfur in melt inclusions from São Miguel, Azores. *Chem Geol* 458.

795 Salters, V.J.M., Stracke, A., 2004. Composition of the depleted mantle. *Geochem*
796 *Geophys Geosy* 5.

797 Sibuet, J.C., Yeh, Y.C., Lee, C.S., 2016. Geodynamics of the South China Sea.
798 *Tectonophysics* 692, 98–119.

799 Sobolev, A.V., Hofmann, A.W., Jochum, K.P., Kuzmin, D.V., Stoll, B., 2011. A
800 young source for the Hawaiian plume. *Nature* 476, 434-U483.

801 Stracke, A., Bizimis, M., Salters, V.J.M., 2003. Recycling of oceanic crust:
802 quantitative constraints. *Geochem Geophys Geosy* 4, 8003.

803 Stracke, A., Hofmann, A.W., Hart, S.R., 2005. FOZO, HIMU, and the rest of the
804 mantle zoo. *Geochem Geophys Geosy* 6.

805 Sun, S.-S., McDonough, W.F., 1989. Chemical and isotopic systematics of oceanic
806 basalts: implications for mantle composition and processes. Geological Society,
807 London, Special Publications 42, 313-345.

808 Tao, K., Grand, S.P., Niu, F., 2018. Seismic Structure of the Upper Mantle Beneath
809 Eastern Asia From Full Waveform Seismic Tomography. *Geochem Geophys*
810 *Geosy* 19, 2732-2763.

811 van der Hilst, R.D., Widiyantoro, S., Engdahl, E.R., 1997. Evidence for deep mantle
812 circulation from global tomography. *Nature* 386, 578-584.

813 Wang, X.C., Li, Z.X., Li, X.H., Li, J., Xu, Y.G., Li, X.H., 2013. Identification of an
814 ancient mantle reservoir and young recycled materials in the source region of a
815 young mantle plume: Implications for potential linkages between plume and
816 plate tectonics. *Earth Planet Sc Lett* 377, 248-259.

817 Wang, Y.J., Han, X.Q., Luo, Z.H., Qiu, Y.Z., Ding, W.W., Li, J.B., Gao, S.T., Chen,
818 R.H. 2009. Late Miocene magmatism and evolution of Zhenbei-Huangyan
819 Seamount in the South China Sea: evidence from petrochemistry and
820 chronology. *Acta Oceanol Sin* 31, 93-102.

821 Workman, R.K., Hart, S.R., 2005. Major and trace element composition of the
822 depleted MORB mantle (DMM). *Earth Planet Sc Lett* 231, 53-72.

823 Wu, H.H., Tsai, Y.B., Lee, T.Y., Lo, C.H., Hsieh, C.H., Toan, D.V., 2004. 3-D Shear
824 Wave Velocity Structure of the Crust and Upper Mantle in South China Sea and
825 its Surrounding Regions by Surface Wave Dispersion Analysis. *Mar Geophys*
826 *Res* 25, 5–27.

827 Yan, Q., Shi, X., Metcalfe, I., Liu, S., Xu, T., Kornkanitnan, N., Sirichaiseth, T.,
828 Yuang, L., Zhang, Y., Zhang, H., 2018. Hainan mantle plume produced late
829 Cenozoic basaltic rocks in Thailand, Southeast Asia. *Sci. Rep.* 8, 2640.

830 Zhang, G.-L., Luo, Q., Zhao, J., Jackson, M.G., Guo, L.-S., Zhong, L.-F., 2018.
831 Geochemical nature of sub-ridge mantle and opening dynamics of the South
832 China Sea. *Earth Planet Sc Lett* 489, 145-155.

833 Zhao, D.P., Yu, S., Ohtani, E., 2011. East Asia: Seismotectonics, magmatism and
834 mantle dynamics. *J. Asian Earth Sci.* 40, 689–709.

835 Zindler, A., Hart, S., 1986. Chemical Geodynamics. *Annu Rev Earth Pl Sc* 14,
836 493-571.

837 Zou, H.B., Fan, Q.C., 2010. U-Th isotopes in Hainan basalts: Implications for
838 sub-asthenospheric origin of EM2 mantle endmember and the dynamics of
839 melting beneath Hainan Island. *Lithos* 116, 145-152.

Fig. 1

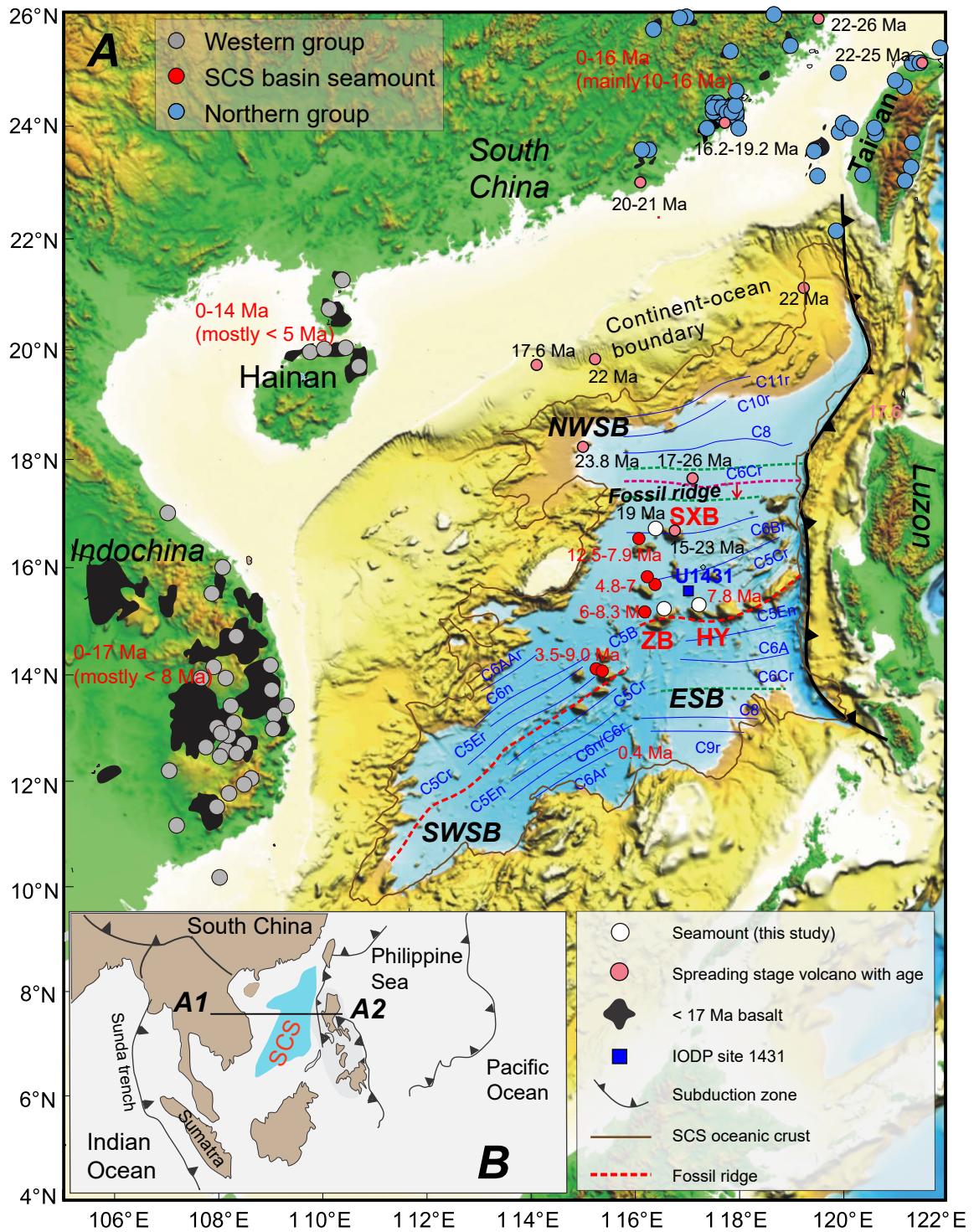


Fig. 2

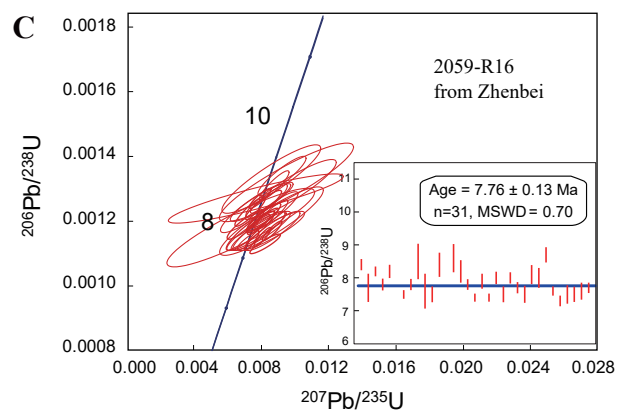
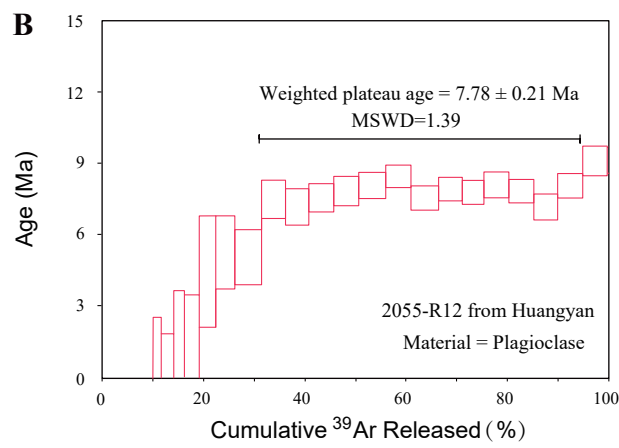
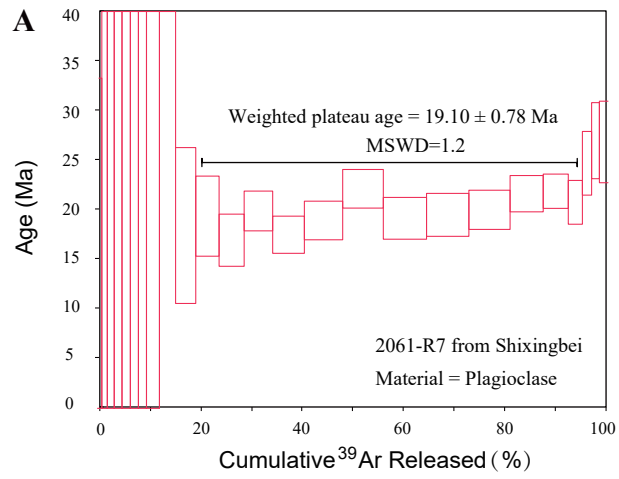


Fig. 3

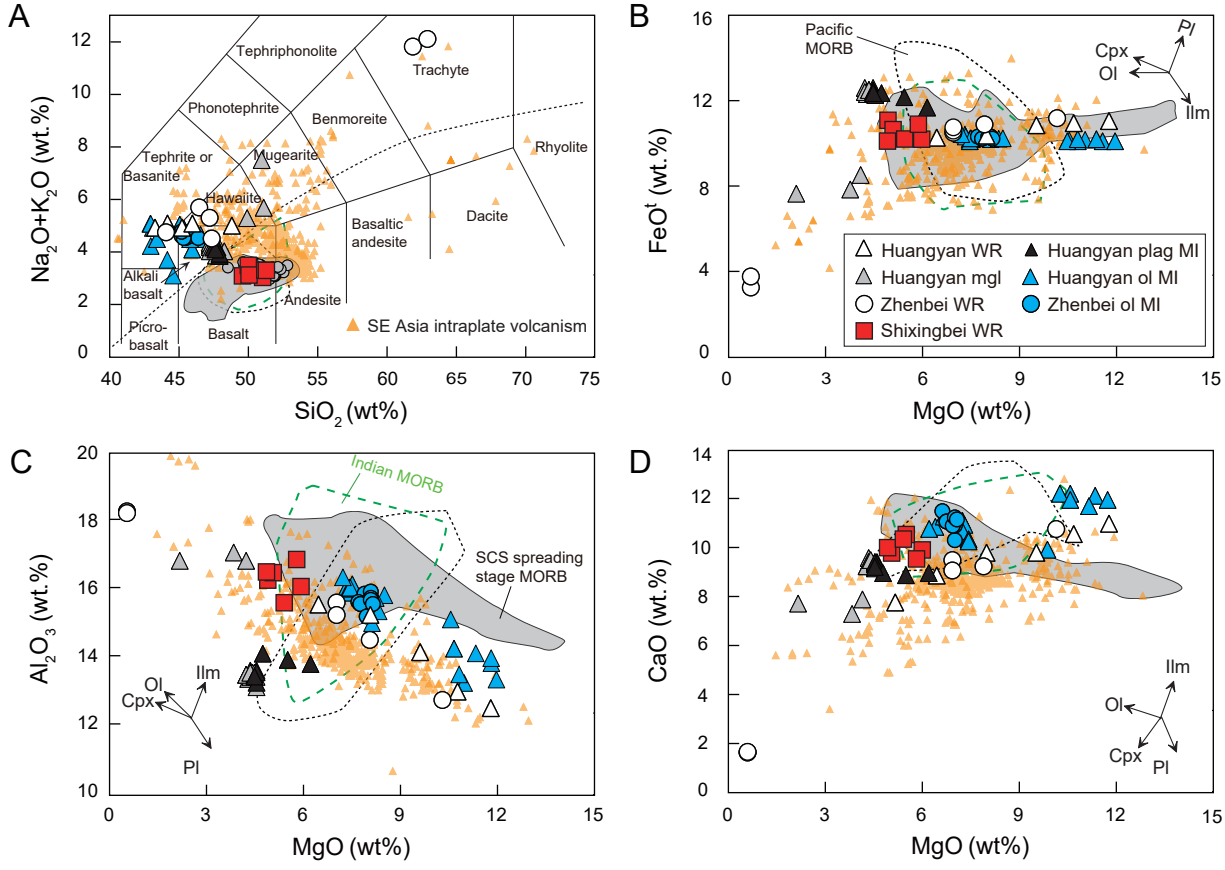


Fig. 4

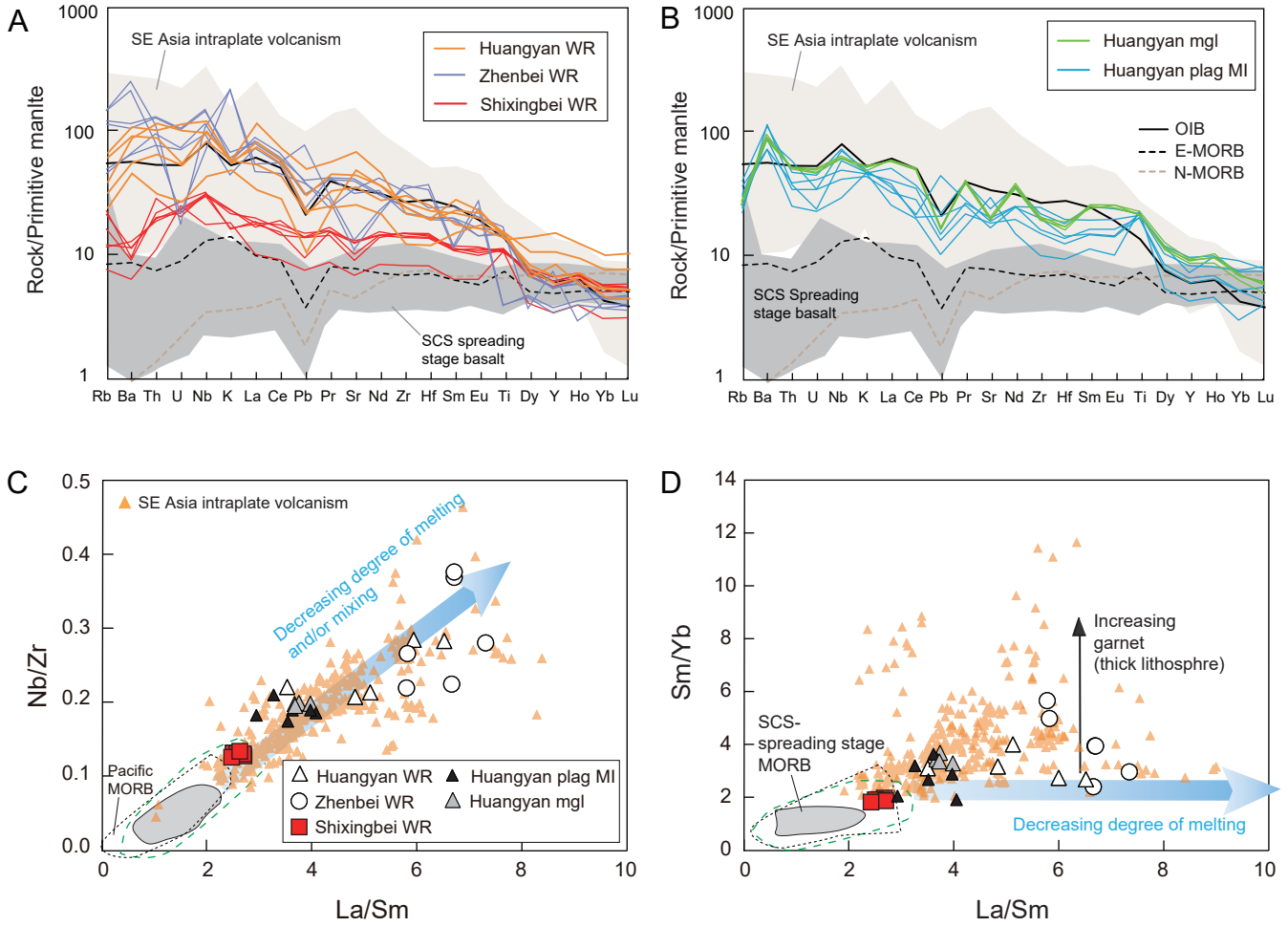


Fig. 5

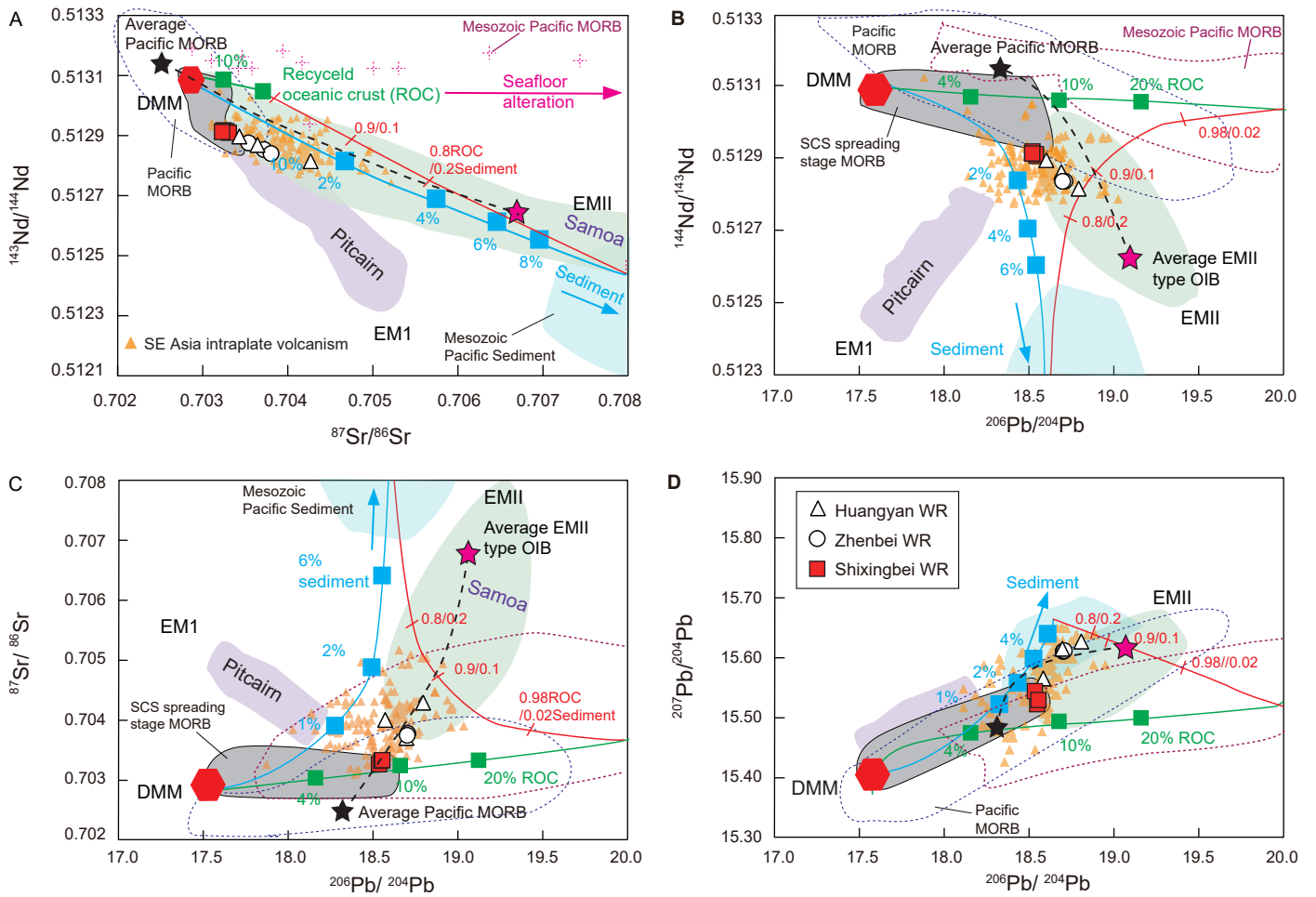


Fig. 6

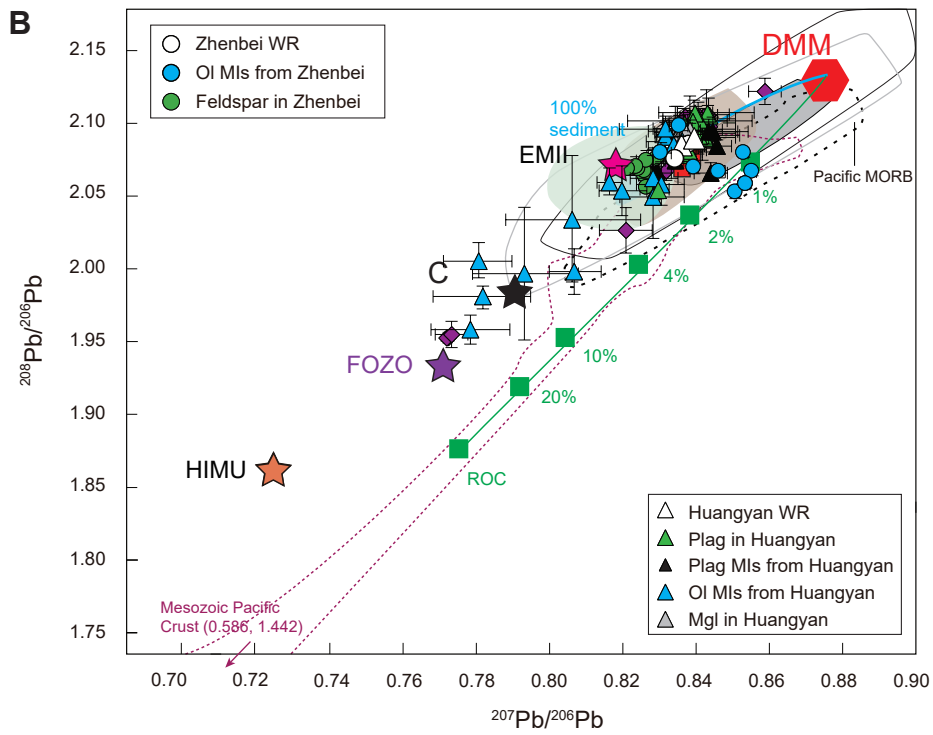
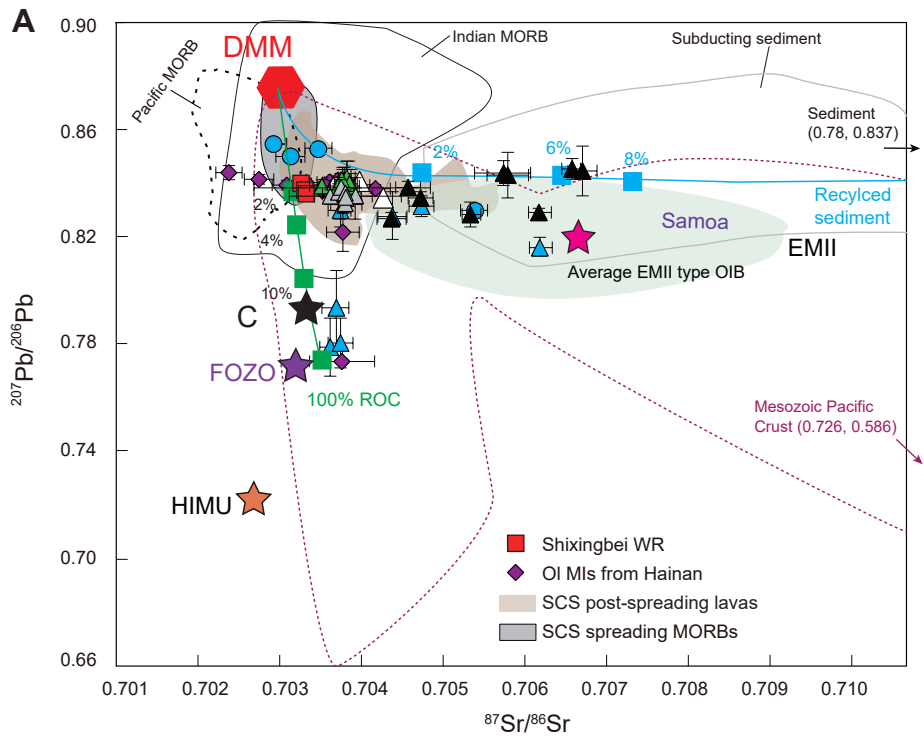


Fig. 7

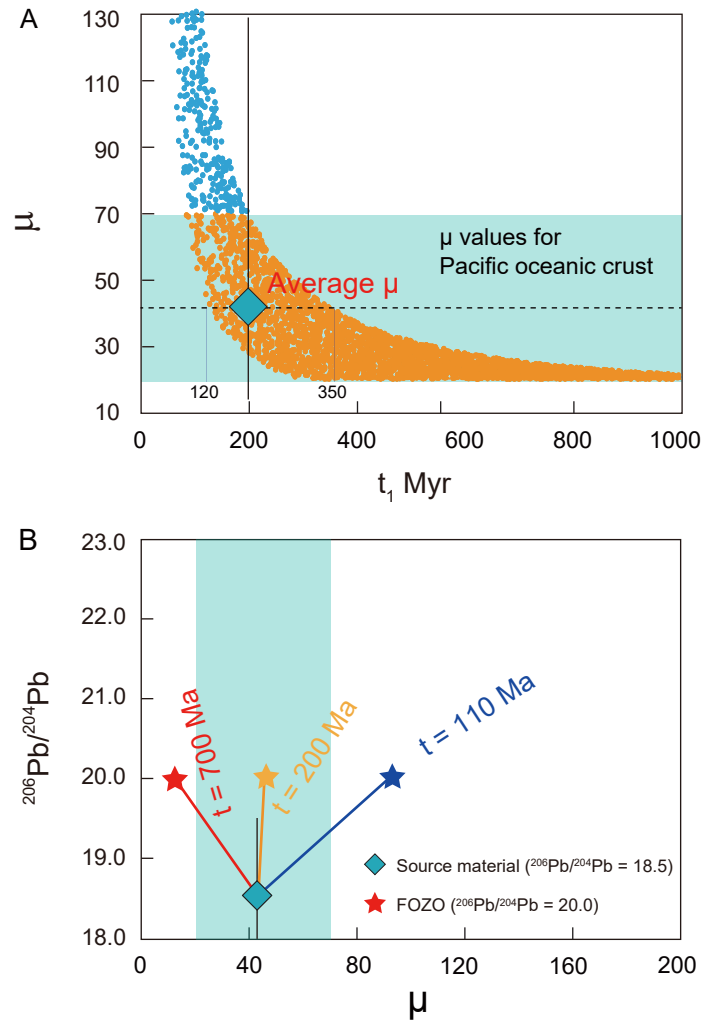


Fig. 8

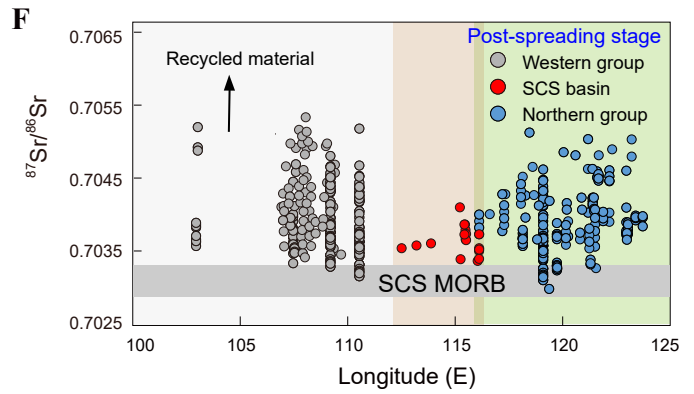
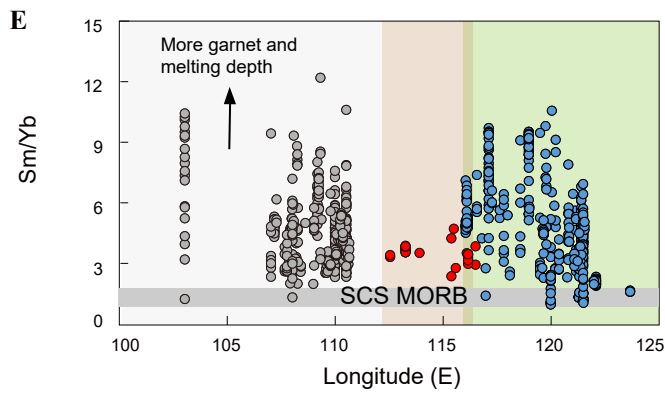
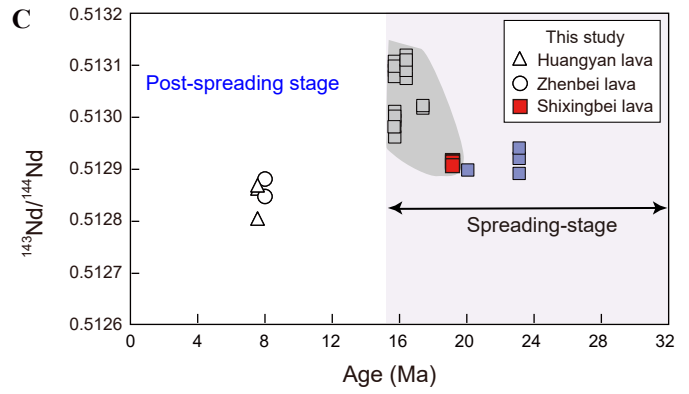
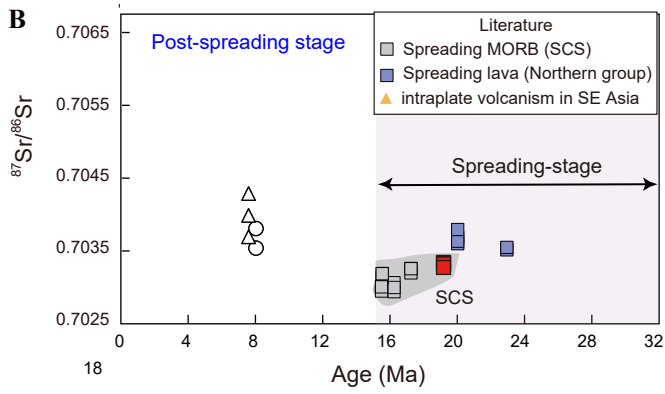
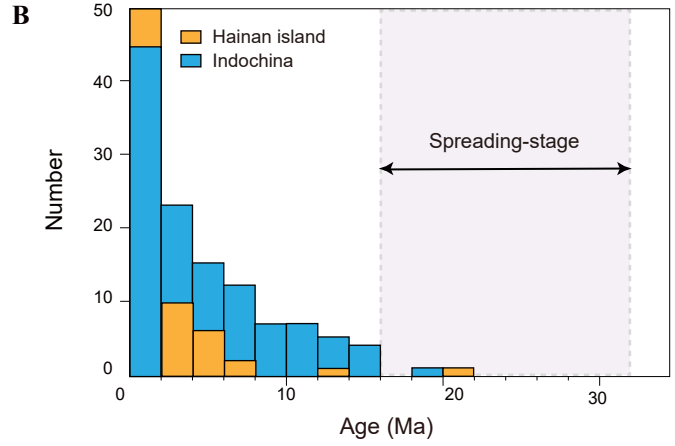
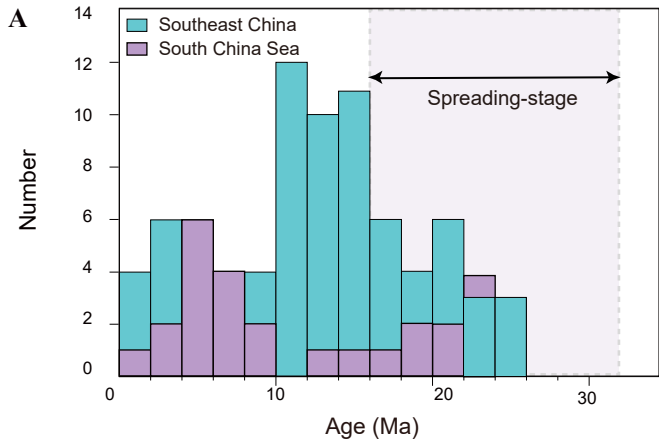


Fig. 9

